

Electronic Supplementary Information for

Resolving the backbone tilt of crystalline poly(3-hexylthiophene) with resonant tender X-ray diffraction

G. Freychet, P. Chantler, Y. Huang, W. L. Tan, M. Zhernenkov, N. Nayak, A. Kumar, P. A. Gilhooly-Finn, C. B. Nielsen, L. Thomsen, S. Roychoudhury, H. Siringhaus, D. Prendergast, and Christopher R. McNeill*

Further experimental details

Sample preparation

Different batches of P3HT were studied to account for a possible influence of molar mass on the observed resonant diffraction data. A commercial batch of P3HT from BASF (P200) was used with molar mass of $M_n = 10$ kg/mol, $D = 1.6$ and regioregularity of greater than 98% along with different batches of “defect free” P3HT¹ produced at the Indian Institute of Technology Bombay (IITB) with molar mass varying from $M_n = 18$ kg/mol to 55 kg/mol. For mechanically aligned (rubbed) samples used for measuring anisotropic X-ray absorption, a similarly produced batch of defect free P3HT synthesized at Queen Mary University London (QMUL) was used with $M_n = 49$ kg/mol and $D = 1.5$. A summary of the sample properties can be found in Table S1.

Table S1. Details of batches of P3HT used in this study.

M_n (kg/mol)	M_w (kg/mol)	D	RR (%)	Source	Film Thickness (nm)	Used for
10	26	1.6	> 98	BASF	Various	Resonant diffraction, NEXAFS
18	27	1.5	100	IITB	300	Resonant diffraction
26	37	1.4	100	IITB	400	Resonant diffraction
55	88	1.6	100	IITB	320	Resonant diffraction
49	74	1.5	100	QMUL	60	Aligned samples for NEXAFS

Samples for resonant diffraction experiments in general were prepared by dissolving P3HT in chloroform and spin-coating onto glass substrates pre-coated with a layer of sodium polystyrene sulfonate (NaPSS). This layer of NaPSS (spin-coated from an aqueous solution at 50 mg/mL and then dried in air at 150 °C) was used as a water sacrificial layer to aid floating

of films after thermal annealing. Following spin-coating of the P3HT layer, samples were transferred to a nitrogen glove box where thermal annealing was performed. Samples were typically annealed to 250 °C which resulted in melting of the sample confirmed by a color change from dark purple to bright orange. The samples were then cooled at a rate of 1 °C per minute until 150 °C after which the hot plate was turned off and the samples left on the hotplate until the temperature reached 100 °C at which point the samples were quenched to room temperature by placing on the metal floor of the glove box. Samples were also prepared from chlorobenzene to produce thinner films, and some samples were also annealed at 180 °C followed by quenching to room temperature. Thicker melt-annealed samples produced data with better signal to noise that was necessary for reliable analysis of anisotropic scattering effects. After annealing, samples were delaminated by floating off onto deionized water and transferred to silicon nitride membranes (Norcada, 200 nm thick membrane, 2 mm × 2 mm window size).

Aligned samples were prepared by spin-coating a polymer solution (1500 rpm, 10 mg mL⁻¹) in ortho-dichlorobenzene on NaPSS-coated glass substrates at 60 °C in a nitrogen glovebox (MBRAUN, <1 ppm O₂, H₂O). Spin-coated films were then annealed at 180 °C for 20 min, and cooled down to room temperature slowly. Polymer alignment was performed by using a RM-50 rubbing machine (E.H.C Co., Ltd.) consisting of a translating stage where the sample was fixed by vacuum and heated at 180 °C located in a separate nitrogen glovebox (Belle Technology, <5 ppm O₂, < 10 ppm H₂O). After rubbing, the samples were transferred back to the original MBRAUN glovebox for a 20 min post-alignment annealing at 180 °C.

Tender X-ray scattering measurements

Resonant tender X-ray scattering measurements were performed at the at the Soft Matter Interfaces (SMI) beamline (Beamline 12-ID) at the National Synchrotron Light Source II.² Measurements were performed in vacuum using a transmission geometry as schematically shown in Figure 2(d), with X-ray polarized in the horizontal direction and samples mounted vertically. X-ray scattering patterns were recorded on a Pilatus 300 K–W detector, consisting of 0.172 mm square pixels in a 1475 × 195 array, mounted at a fixed distance of 0.275 m from the sample position. To cover the range of scattering angles desired, the vertically oriented elongated detector was moved horizontally on a fixed arc and images were later visualized in Xi-CAM software³ and stitched using custom code. Scattering patterns were measured as a function of energy by varying the photon energy between 2445 and 2500 eV, with steps of 0.25 eV taken through the sulfur K-edge between 2470 and 2480 eV. The sample was moved to a

fresh spot for each new energy to avoid beam damage. The spot size at the sample was 20 μm by 200 μm .

Data reduction and analysis

Two-dimensional scattering data were reduced to one-dimensional scattering profiles by either radially averaged the data or performing sector averages of width $\pm 15^\circ$ along q_{hor} (parallel to E) or q_{ver} (perpendicular to E) as defined by Figure 2(d). Peak fitting was performed using an automated routine implemented in Igor Pro utilizing the multi-peak fitting function. Peak fitting was performed over a q range of 0.30 \AA^{-1} to 0.45 \AA^{-1} with a single Voigtian peak used in conjunction with a linear baseline. Example peak fits are shown in **Figure S1**.

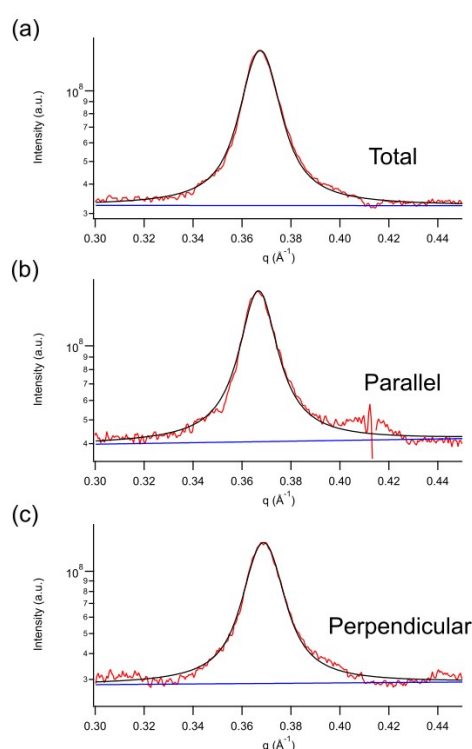


Figure S1. Example peak fits to the (100) peak using a linear background and single Voigtian peak: (a) Radially averaged data; (b) profile along the direction parallel to E ; (c) profile along the direction perpendicular to E . Data shown corresponds to the sample show in Figure 2 in the main manuscript taken at an energy of 2450 eV.

Hard X-ray GIWAXS

Grazing incidence wide angle X-ray scattering measurements using hard X-rays were performed at the SAXS/WAXS beamline at the Australian Synchrotron.⁴ Scattering patterns were collected on a two-dimensional Dectris Pilatus3 2M in-vacuum detector with pixel size of 0.172 mm \times 0.172 mm placed 628 mm downstream from the sample stage. The sample stage and detector and indeed the entire beam path was enclosed in a vacuum chamber to minimize

background air scatter. An exposure of 1 s was used, with three 1 s exposures taken at different lateral offsets to cover the gaps between detector modules. These three exposures were combined to create a smooth 2D image. A fresh spot on the sample was used for each incident angle to prevent beam damage. GIWAXS data were processed using a modified version of the Nika package implemented within IgorPro.⁵

X-ray absorption spectroscopy

Near-edge X-ray absorption fine structure (NEXAFS) spectroscopy was performed either at the SMI beamline with the two dimensional area detector acting as a fluorescence detector, or at the Soft X-ray beamline at the Australian Synchrotron.⁶ For measurements at the SMI beamline, for every resonant diffraction experiment a NEXAFS spectrum is acquired by using the background intensity as a measure of the X-ray fluorescence, with further details provided in our previous publication.⁷ Measurements at the Soft X-ray beamline were performed using partial electron yield (PEY) mode where a channeltron detector was used to measure the electrons ejected from the sample following X-ray absorption. Samples for measurement at the Soft X-ray beamline were prepared on highly doped silicon wafers. For data acquired at the Australian Synchrotron, processing and analysis was performed using QANT,⁸ with further details of normalization provided elsewhere.⁹ Fluorescence yield (FY) and PEY measurements resulted in equivalent data, with a comparison provided in **Figure S2**.

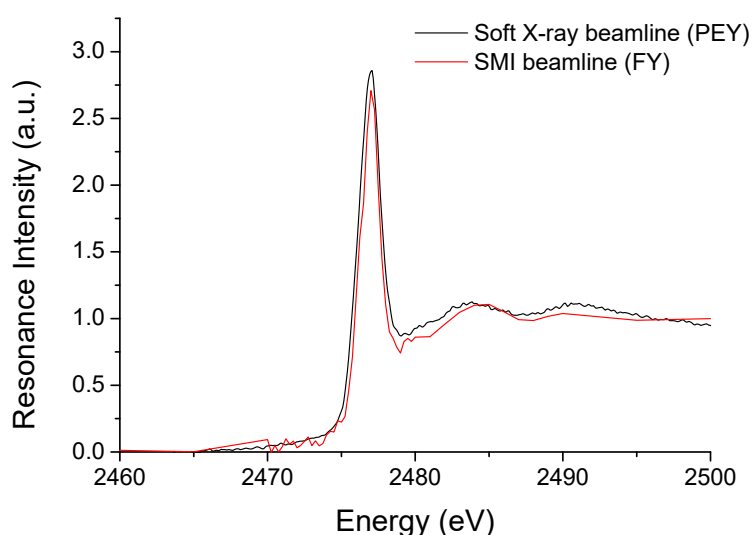


Figure S2. Comparison of PEY NEXAFS data taken at the Soft X-ray beamline at the Australian Synchrotron and FY NEXAFS data taken at the SMI beamline at the NSLS-II. Data shown is of a spin-coated sample measured with the X-ray beam incident normal to the sample. The energy scale of the PEY data has been adjusted to match the energy scale of the SMI beamline.

Determination of atomic scattering factors

Atomic scattering factors were calculated using KKCalc.¹⁰ Using this program, the pre-edge and post-edge regions of a sulfur K-edge NEXAFS spectrum can be scaled to the known, calibrated X-ray absorption cross sections of sulfur. The absolute atomic scattering factors f' and f'' of the sulfur atoms can then be computed by KKCalc, with a Kramers-Kronig transformation used to convert between f'' and f' , noting that $f' = Z - f_1$ and $f'' = f_2$ where Z is the atomic number. For the carbon and hydrogen atoms in the sample, tabulated values for the atomic scattering factors of these atoms were used.

Simulations of resonant diffraction profiles

Simulations of resonant diffraction profiles were performed using custom code implemented in MatLab. This code uses atomic position data (expressed in fractional coordinates) based on a proposed unit cell, r_i , and the complex energy dependent scattering factor $f_i = f_0 + f' + if''$ as inputs to calculate the complex structure factor of a particular reflection $h = (h,k,l)$:

$$F(h) = \sum_i^{atoms} f_j \exp(2\pi h \cdot r_j) \quad (S1)$$

The energy dependent diffraction intensity is then calculated as:

$$I(h) = |F(h)|^2 \quad (S2)$$

Resonant diffraction data of films of different thickness

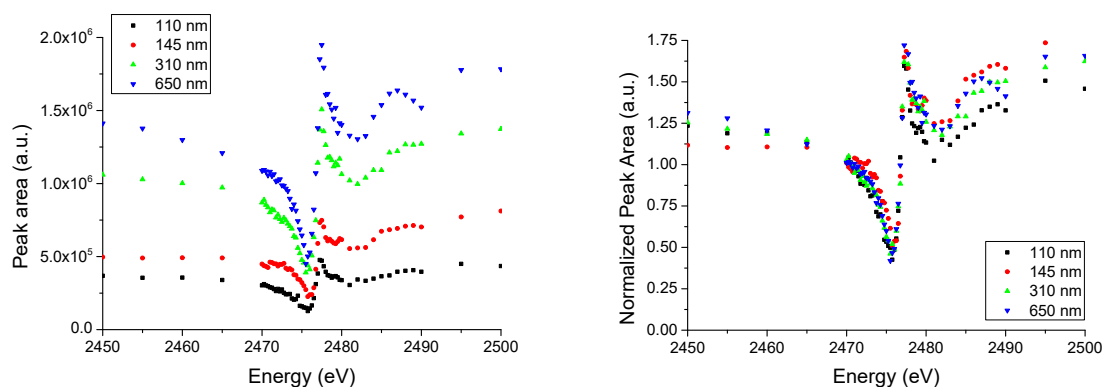


Figure S3. Plots of radially averaged (100) peak area as a function of energy for films of different thickness. The left plot shows the raw data while right graph compares to normalized data showing that films of different thickness give very similar resonant diffraction profiles. The two thinner samples were spin-coated from chlorobenzene while the two thicker samples were spin-coated from chloroform. Samples in this case were annealed at 180 °C.

Grazing incidence wide-angle X-ray scattering data

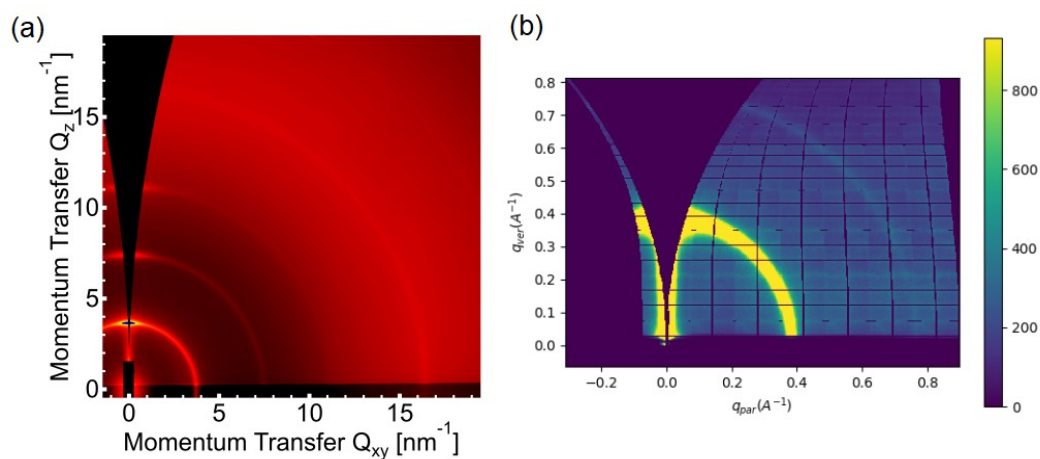


Figure S4. GIWAXS data of the 10 kg/mol sample shown in Figure 2 taken at (a) 15.2 keV and (b) 2.45 keV.

Resonant diffraction data of films of different molar mass

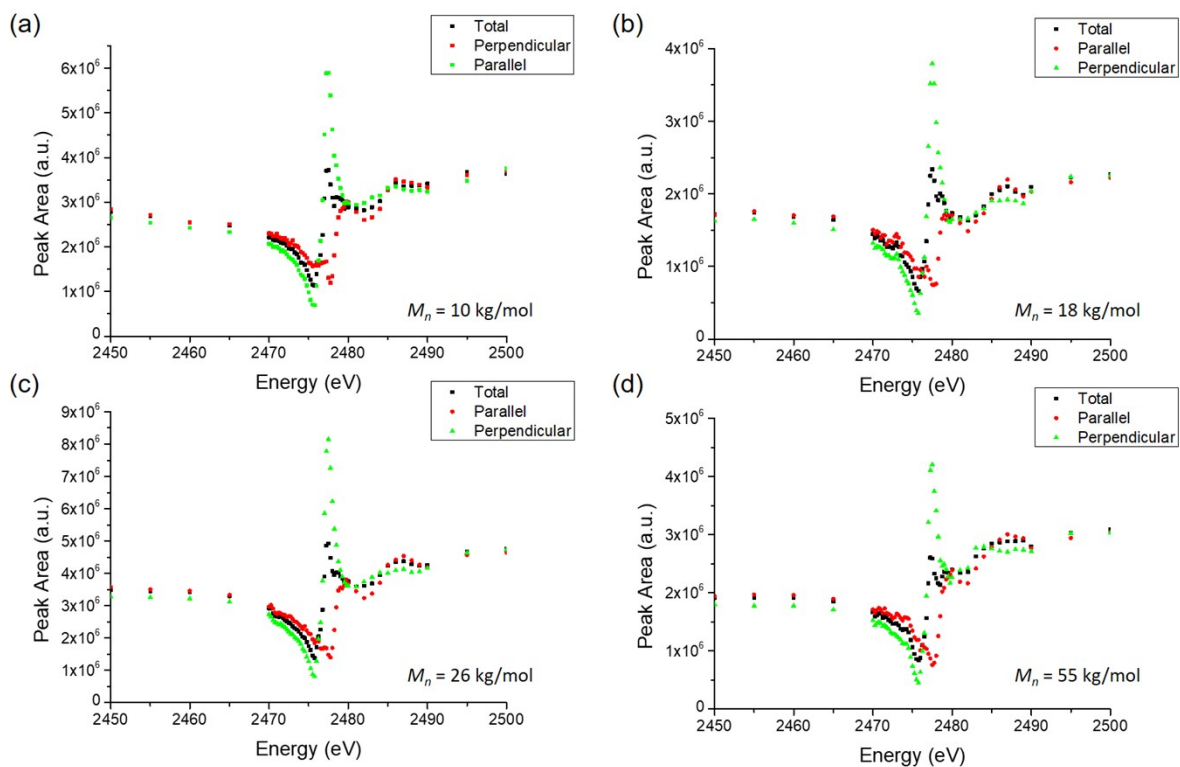


Figure S5. Resonant diffraction profiles taken of samples with different molar mass. (a) $M_n = 10$ kg/mol (500 nm thick); (b) $M_n = 18$ kg/mol (300 nm thick); (c) $M_n = 26$ kg/mol (400 nm thick); (d) $M_n = 55$ kg/mol (320 nm thick).

Figure S5 shows the resonant diffraction data of samples of different molar mass. In general the different data sets are consistent accounting for noise and other experimental variabilities. Furthermore, no systematic changes with molar mass are seen which would indicate a molecular weight dependence of the resonant diffraction behaviour.

Calculated resonant diffraction profiles on absolute scale

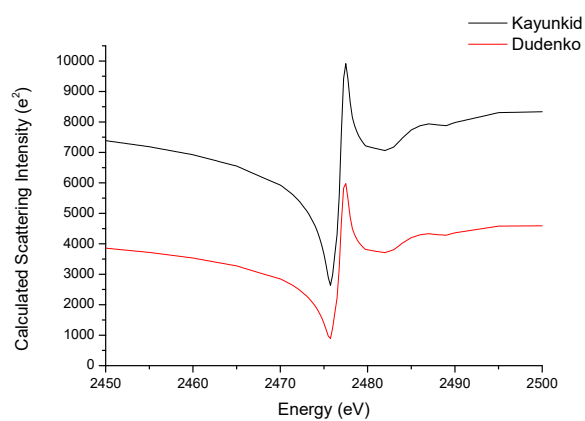


Figure S6. Comparison of the calculated radially-averaged resonant diffraction profiles according to the Kayunkid and Dudenko unit cells on an absolute scattering intensity scale.

Details of first-principles calculations

Simulation of the absorption spectra was performed using the Many-Body X-ray Absorption Spectroscopy (MBXAS) method¹¹⁻¹³ which computes the transition amplitudes from the dipole approximation of Fermi's Golden rule by approximating each many-electron state as a single Slater determinant. In particular, the determinant pertaining to the initial (final) state is constructed using Kohn-Sham¹⁴ orbitals obtained from a density-functional theory^{14, 15} (DFT) based self-consistent field calculation performed in presence (absence) of the relevant core electron. The effects of the core-hole are included with the help of a modified pseudopotential. In order to incorporate the difference in the chemical environment of the excited sulfur atoms (in the same or different systems), the spectra were aligned with the help of a computational scheme reliant on formation-energy differences.^{16, 17} Additionally, a rigid shift of 2471.5 eV (dependent on the pseudopotentials used) was applied on all spectra to align them with the experimental counterparts. The DFT calculations were performed with the Quantum-ESPRESSO¹⁸ software package, using the Perdew-Burke-Ernzerhof (PBE)^{19, 20} functional in conjunction with ultrasoft pseudopotentials.²¹ A plane-wave cutoff of 25 eV (200 eV) was used for calculating the electronic wave-function (density).

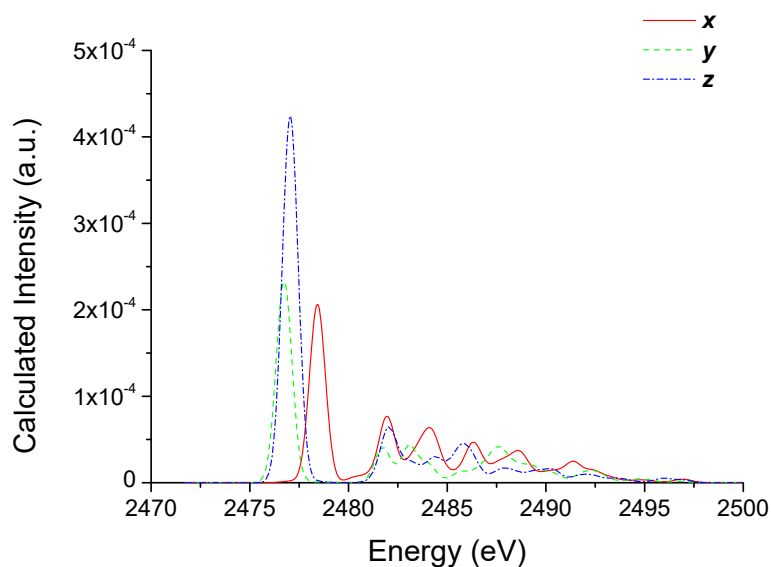


Figure S7. X-ray absorption spectra of gas phase thiophene calculated from first principles.

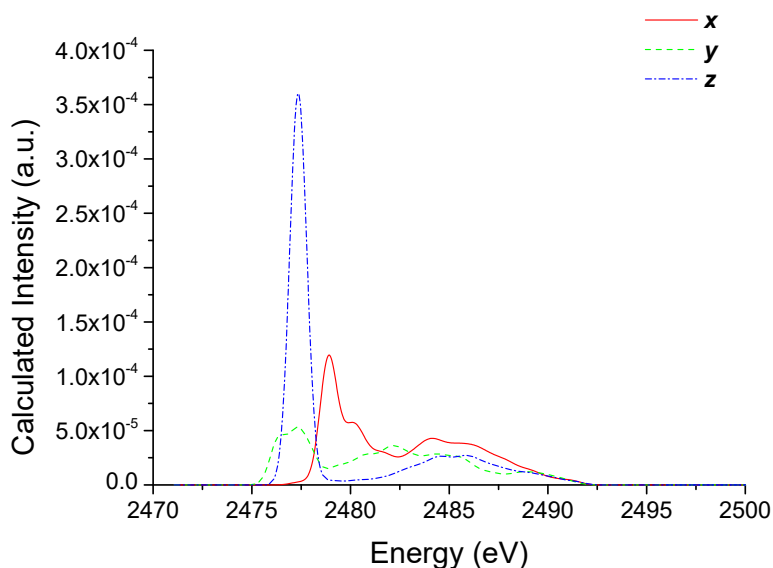


Figure S8. X-ray absorption spectra of crystalline P3HT performed using atomic positions from the Dudenko unit cell.

Determination of the anisotropic atomic scattering factors

To account for the anisotropy observed in the resonant X-ray diffraction data, knowledge of the anisotropic X-ray optical properties is required. The X-ray absorption spectra of P3HT at the sulfur K-edge corresponding to polarization of the X-ray beam parallel to the different molecular axes was determined using a combined experimental and theoretical approach. There are two different coordinate frames that one could consider: that of the crystalline unit cell which are defined by the \mathbf{a} (side chain stacking), \mathbf{b} (π - π stacking) and \mathbf{c} (backbone stacking) axes (see **Figure S9**), and that defined by the planar aromatic backbone of the polymer. For the latter case, in the solid state the P3HT backbone adopts a planar configuration so one can define three molecular axes \mathbf{x} , \mathbf{y} , and \mathbf{z} as defined in **Figure S10**. Axis \mathbf{x} is aligned in the plane of the thiophene rings but perpendicular the backbone axis \mathbf{z} . Axis \mathbf{y} is perpendicular to the plane of the thiophene rings. While axis \mathbf{z} can be assumed to be parallel to lattice vector \mathbf{c} , axis \mathbf{x} is not necessarily parallel to the lattice vector \mathbf{a} , and axis \mathbf{y} is not necessarily parallel to lattice vector \mathbf{b} due to the possible tilting of the backbone within the unit cell. For a perfectly aligned single crystal one can precisely measure NEXAFS spectra corresponding to the cases where the electric field vector is aligned parallel to the three crystallographic axes. Alternatively, first-principles calculations of X-ray absorption spectra can provide calculations of X-ray absorption spectra with the electric field vector aligned parallel to the three molecular axes. Due to the semicrystalline nature of conjugated polymers

it is not easy to produce single crystals. However aligned samples can be produced through techniques such as mechanical rubbing. P3HT films also generally possess an “edge-on” texture. Experimental measurement of aligned and edge-on samples provide experimental NEXAFS spectra corresponding to preferential alignment of polymer chains with respect to the polarization of the X-ray beam. From these experimental spectra and their associated dichroism the X-ray absorption spectra corresponding to alignment of the electric field vector of the X-ray beam parallel to the three molecular axes are determined as described below.

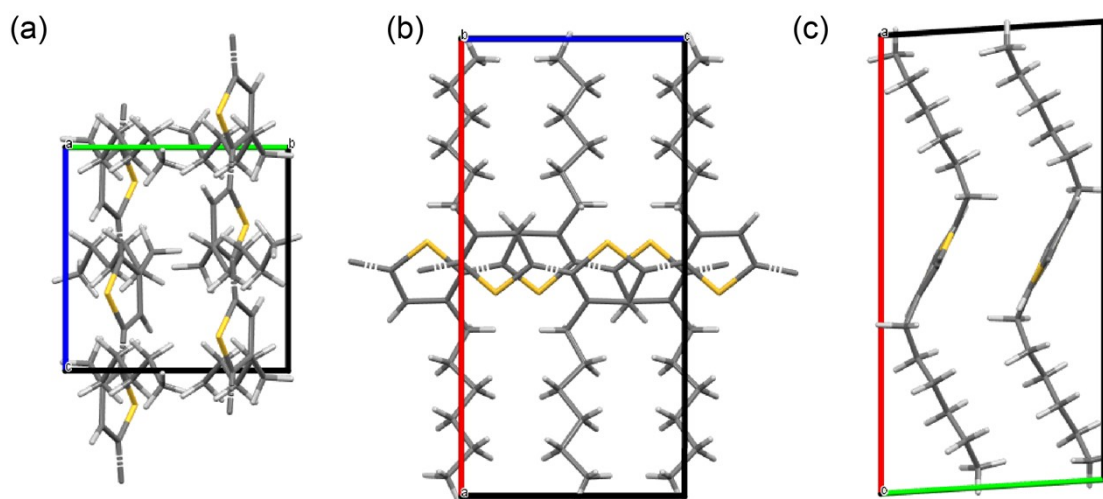


Figure S9. Unit cell axes of a possible crystalline packing of P3HT after Kayunkid et al.²² The side chain stacking direction, a , is shown in red. The π - π stacking direction, b , is shown in green. The backbone stacking direction, c , is shown in blue. Part (a) shows a view looking down the a axis. Part (b) shows a view looking down the b axis. Part (c) shows a view looking down the c axis.

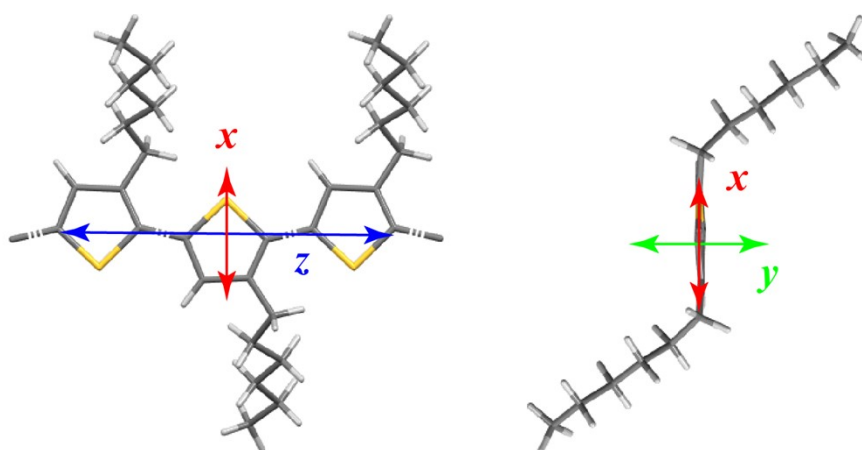


Figure S10. Definition of the molecular axis x , y , and z , of the backbone of P3HT.

By measuring the NEXAFS spectra of highly aligned films one can measure the NEXAFS spectra for different orientations of the polymer backbone with respect to the beam polarization. Highly aligned films were produced by mechanical rubbing as described above. **Figure S11** shows the NEXAFS spectra taken of aligned P3HT films corresponding to different

orientations of the electric field vector with respect to the rubbing direction. The large anisotropy in the data confirms a high degree of polymer chain alignment. Mechanical rubbing produces samples where the backbone is aligned with the rubbing direction, and thus the spectrum taken with the electric field vector aligned parallel to the rubbing direction corresponds to the case where there is preferential alignment of the electric field vector with the backbone axis, either c or z . However as this rubbed sample is not perfectly aligned as the perpendicular spectrum still contains peak intensity at 2477 eV, as shown by the dashed line in **Figure S12(a)**. To correct for this, a difference spectrum was calculated by subtracting the parallel spectrum from the perpendicular spectrum, see **Figure S12(a)**. This difference spectrum can then be used to identify and correct the signal from non-aligned chains and therefore to extrapolate the spectra for an ideally aligned sample.²³ By adding or subtracting 0.2 times this difference spectrum from the measured parallel and perpendicular spectra, the spectra in **Figure S12(b)** were obtained, which are regarded as corresponding to the cases where the \mathbf{E} is parallel and perpendicular to the backbone axis, z . A factor of 0.2 was chosen since the spectrum with \mathbf{E} perpendicular to the backbone contains no peak at 2477 eV. This spectrum should only contain features associated with \mathbf{E} aligned with the x and y , which will subsequently be verified.

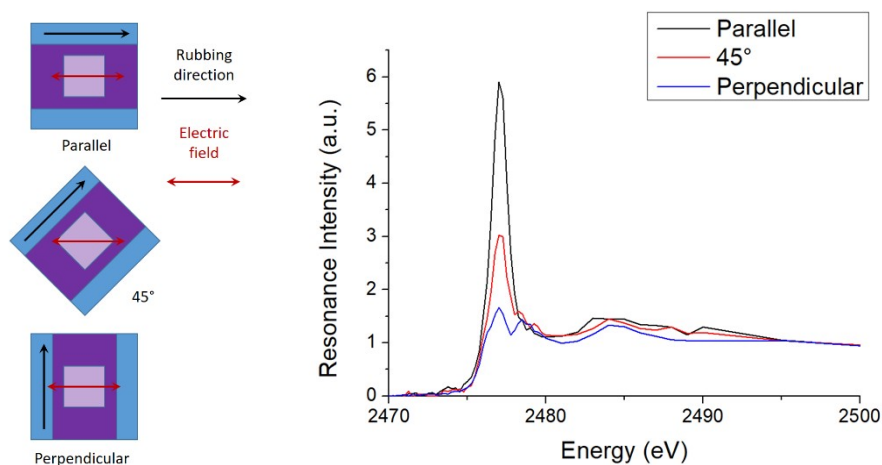


Figure S11. Sulfur K-edge NEXAFS spectra of aligned P3HT films produced by mechanical rubbing for different orientations of the electric field-vector with respect to the rubbing direction. This data was acquired at the SMI beamline in transmission using fluorescence detection.

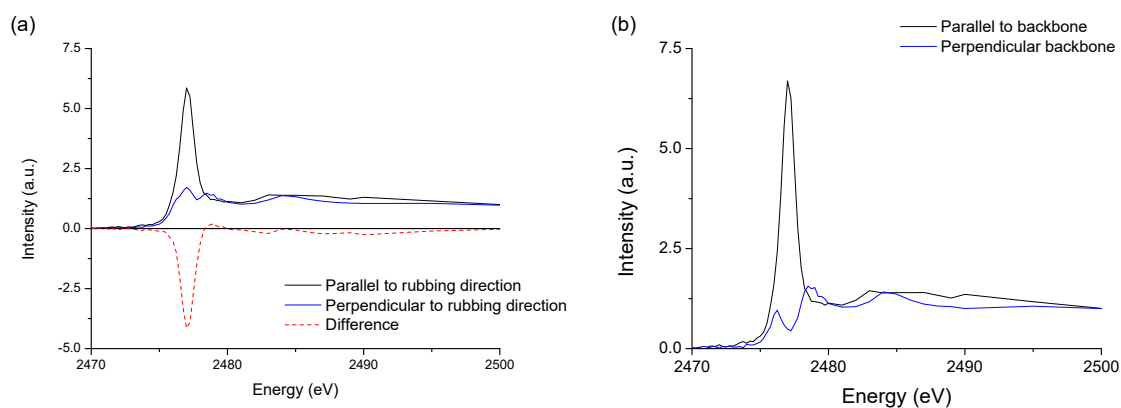


Figure S12. (a) Sulfur K-edge NEXAFS spectra of aligned P3HT films with difference spectrum. The dashed line at 2477 eV corresponds to the energy of the dominant backbone peak. (b) Extrapolated NEXAFS spectra corresponding to polarization parallel and perpendicular to the backbone obtained by adding/subtracting 0.2 times the difference spectrum to the parallel and perpendicular spectra in part (a).

While mechanical rubbing was found to produce aligned films of P3HT with a high degree of in-plane backbone alignment, the aligned films exhibited a mixture of edge-on and face-on alignment with respect to the substrate. This mixed edge-on/face-on orientation made it difficult to acquire spectra with the electric field vector preferentially aligned with either the side chain stacking direction or the π - π stacking direction. Spin-coated P3HT films annealed at 180 °C however do exhibit preferentially edge-on samples which were measured with different orientations of the incident electric field vector with respect to the substrate, see **Figure S13**, **Figure S14**. For an angle of incidence of 90°, the X-ray beam is incident normal to the substrate with electric field vector parallel to the substrate. A NEXAFS spectrum acquired at normal incidence on a spin-coated film with no preferential in-plane alignment will strongly resonate with transitions parallel to the π - π stacking direction and parallel to the backbone direction. For an angle of incidence of 20°, the electric field vector is mostly aligned perpendicular to the substrate and thus preferentially aligned with the side chain stacking direction. The spectrum acquired at 20° however cannot be taken as being perfectly aligned with either the axis a or the axis x due to: (i) the angle of incidence of 20° is not perfectly parallel to the substrate plane, (ii) the sample is not necessarily perfectly edge-on. As above, by calculating a difference spectrum (i.e. subtracting the spectrum acquired at 20° from the one acquired at 90°) one can identify the underlying resonant transitions and their associated dichroism,²³ enabling the measured spectra to be extrapolated. From the first-principles calculations, the spectrum corresponding to alignment with the polarization along x axis should correspond to the case when there is zero resonance intensity below 2478 eV, with transitions below this energy requiring polarization oriented perpendicular to x . The difference spectrum clearly reveals the presence of three characteristic peaks at ~2477 eV, 2478.5 eV and 2484 eV.

By subtracting a factor of 0.8 times the difference spectrum from the 20° spectrum yields a spectrum with no resonance intensity at 2477 eV, **Figure S14(c)**. This spectrum is then taken as the principal spectrum corresponding to E parallel to x .

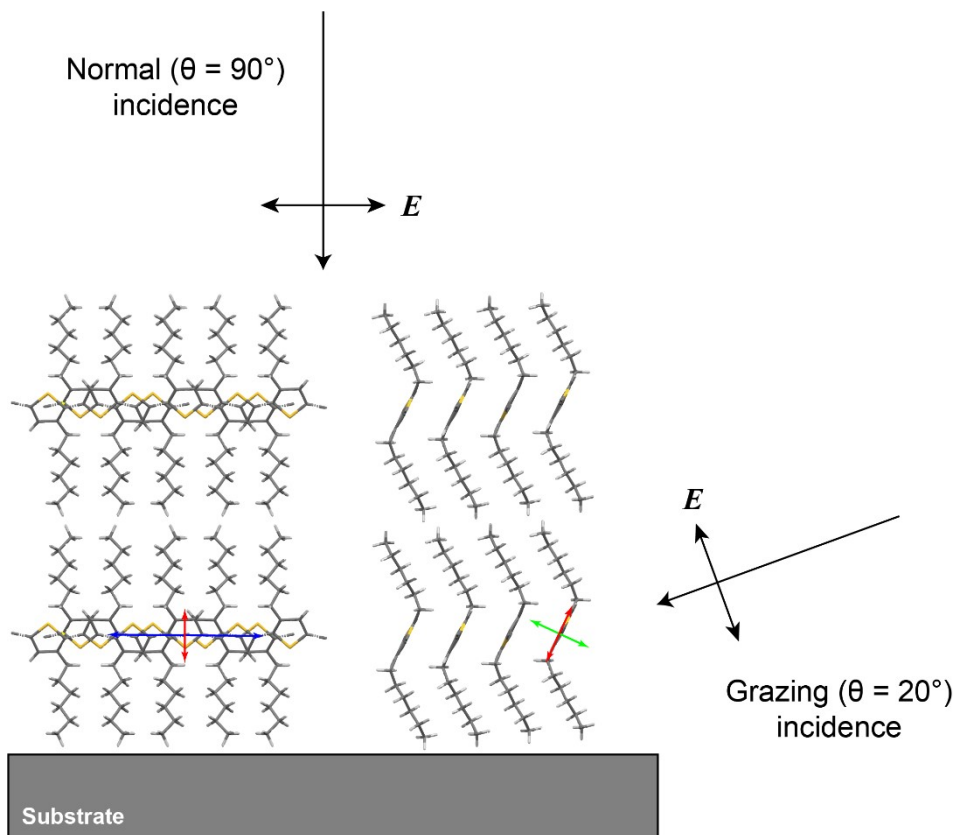


Figure S13. Geometry of the angle-resolved NEXAFS spectroscopy experiment of edge-on spin-coated films. Note that the sample lacks macroscopic in-plane alignment of polymer backbones meaning that the beam is sampling all possible azimuthal orientations of backbones within the plane of the film.

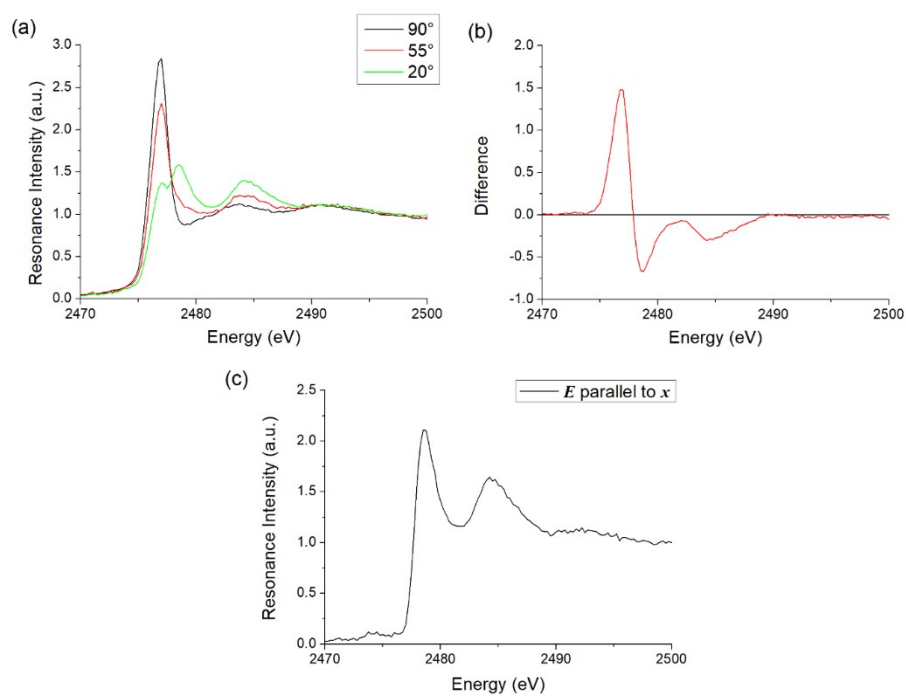


Figure S14. (a) Angle-resolved PEY NEXAFS spectra taken at different polar angles. (b) Difference spectrum computed by subtracting the 20° spectrum in (a) from the 90° spectrum in (a). (c) Corrected spectrum corresponding to the situation where the electric field vector is parallel to axis x with zero resonance intensity at energies below 2477 eV.

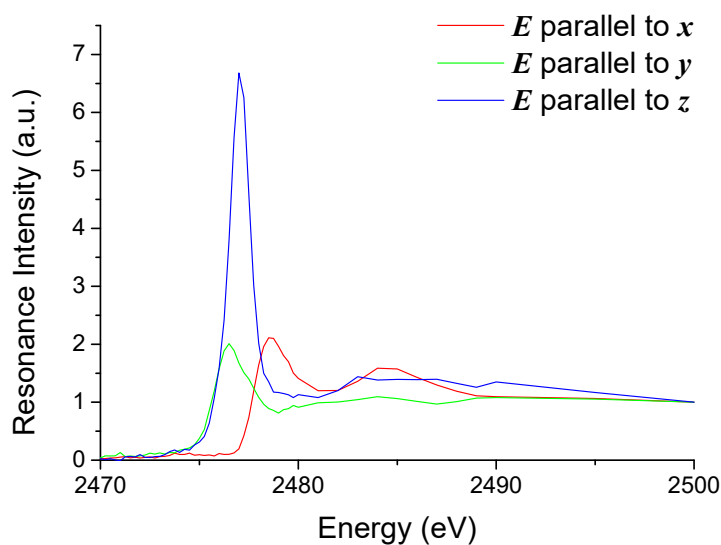


Figure S15. Experimentally derived principal sulfur K-edge NEXAFS spectra of P3HT.

With knowledge of the spectra corresponding to E parallel to x and corresponding to E parallel to z , it is possible to recreate the spectrum corresponding to E parallel to y . This can be achieved by recognizing that any spectrum acquired will represent a linear combination of the three principal spectra. For example, for a spectrum acquired at the magic angle (55° for a spin-

coated sample) the spectrum should have roughly equal contributions from each of the principal components. The spectrum corresponding to E parallel to y was then constructed by subtracting equal amounts of the two other principal spectra from the 55° spectrum. This resulted in a spectrum that had unique features including a low energy peak at 2476.5 eV matching the simulated peak expected for this spectrum, with the three principal spectra shown in **Figure S15**. To check the consistency of the approach, the spectrum from **Figure S12(b)** was fit with a linear combination of spectra x and y , with the result shown in **Figure S16**. There is excellent agreement between these two spectra, with the linear fit able to accurately match the experimental features. The principal spectra x , y , and z were then used as the basis for calculating the polarization-dependent f' and f'' .

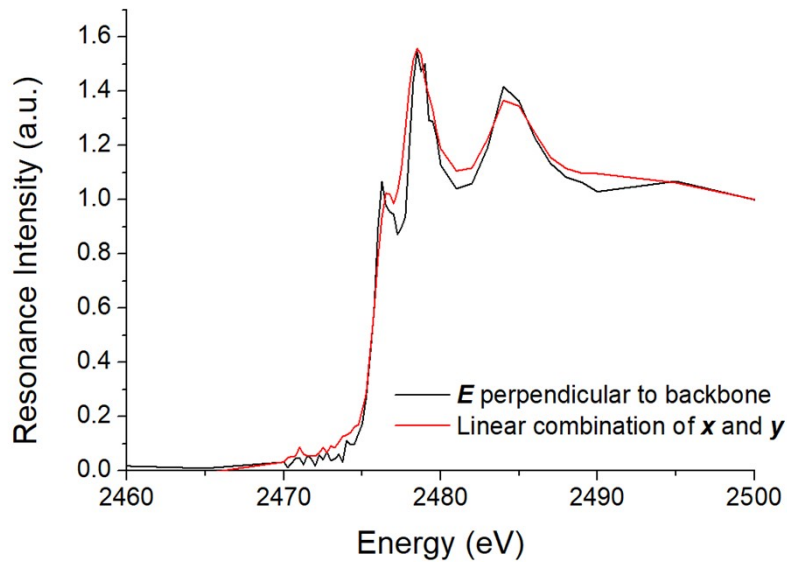


Figure S16. Comparison of the experimental spectrum with E parallel to the backbone direction (from **Figure S12(b)**) to a linear combination of spectra x and y .

Atomic scattering factors as a function of backbone tilt

With the tilting of the planar backbone with respect to the unit cell axes defined by θ_{tilt} as in Figure 7 in the main manuscript, the X-ray absorption spectrum corresponding to E parallel to a (I_a) was formed using a linear combination of the principal spectra I_x and I_y as follows:

$$I_a = \cos^2(\theta_{tilt})I_y + \sin^2(\theta_{tilt})I_x \quad (S3)$$

Figure S17 shows the calculated spectra for different values of θ_{tilt} . I_a was then converted to atomic scattering factors as described previously.

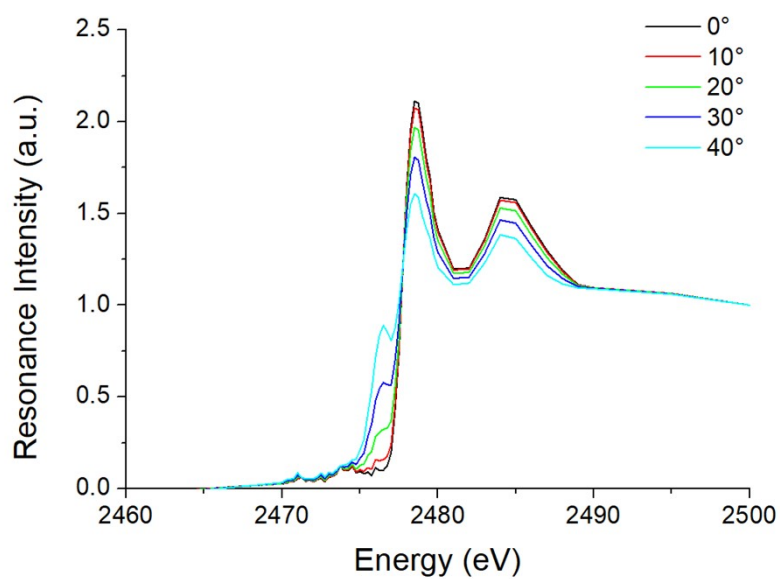


Figure S17. Spectra I_a as a function of backbone tilt angle as determined by Equation S3.

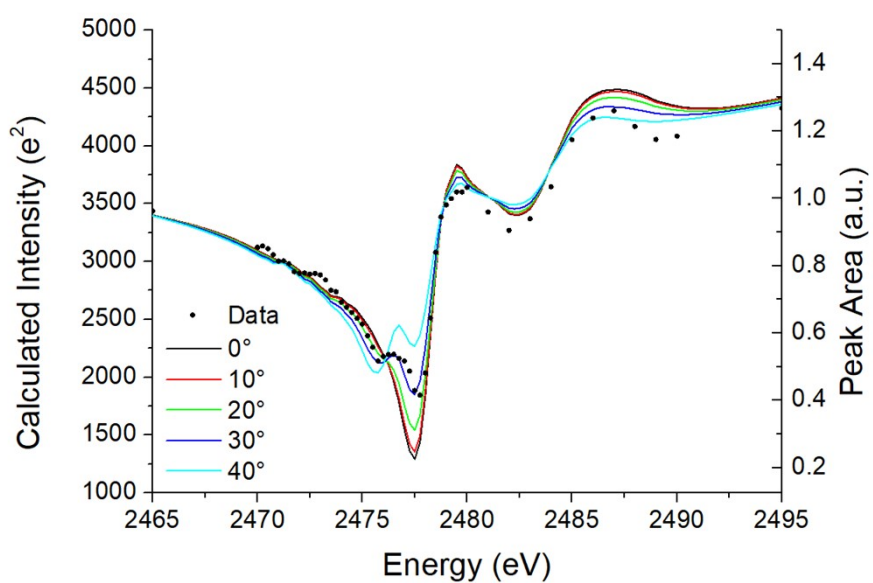


Figure S18. Influence of backbone tilt angle θ_{tilt} on the calculated resonant diffraction profiles using atomic position data from the Dudenko model.²⁴

References

1. A. Nawaz, M. S. Meruvia, D. L. Tarange, S. P. Gopinathan, A. Kumar, A. Kumar, H. Bhunia, A. J. Pal and I. A. Hümmelgen, *Org. Electron.*, 2016, **38**, 89-96.
2. M. Zhernenkov, N. Canestrari, O. Chubar and E. DiMasi, *Proc. SPIE*, 2014, **9209**, 92090G.
3. R. J. Pandolfi, D. B. Allan, E. Arenholz, L. Barroso-Luque, S. I. Campbell, T. A. Caswell, A. Blair, F. De Carlo, S. Fackler, A. P. Fournier, G. Freychet, M. Fukuto, D. Gursoy, Z. Jiang, H. Krishnan, D. Kumar, R. J. Kline, R. Li, C. Liman, S. Marchesini, A. Mehta, A. T. N'Diaye, D. Y. Parkinson, H. Parks, L. A. Pellouchoud, T. Perciano, F. Ren, S. Sahoo, J. Strzalka, D. Sunday, C. J. Tassone, D. Ushizima, S. Venkatakrishnan, K. G. Yager, P. Zwart, J. A. Sethian and A. Hexemer, *J. Synchrotron Rad.*, 2018, **25**, 1261-1270.
4. N. M. Kirby, S. T. Mudie, A. M. Hawley, D. J. Cookson, H. D. T. Mertens, N. Cowieson and V. Samardzic-Boban, *J. Appl. Cryst.*, 2013, **46**, 1670-1680.
5. I. Ilavsky, *J. Appl. Cryst.*, 2012, **45**, 324-328.
6. B. C. C. Cowie, A. Tadich and L. Thomsen, *AIP Conf. Proc.*, 2010, **1234**, 307-310.
7. G. Freychet, E. Gann, L. Thomsen, X. Jiao and C. R. McNeill, *J. Am. Chem. Soc.*, 2021, **143**, 1409-1415.
8. E. Gann, C. R. McNeill, A. Tadich, B. C. C. Cowie and L. Thomsen, *J. Synchrotron Rad.*, 2016, **23**, 374-380.
9. M. M. Nahid, E. Gann, L. Thomsen and C. R. McNeill, *Eur. Polym. J.*, 2016, **81**, 532-554.
10. B. Watts, *Opt. Express*, 2014, **22**, 23628-23639.
11. Y. Liang and D. Prendergast, *Phys. Rev. B*, 2018, **97**, 205127.
12. Y. Liang and D. Prendergast, *Phys. Rev. B*, 2019, **100**, 075121.
13. Y. Liang, J. Vinson, S. Pemmaraju, W. S. Drisdell, E. L. Shirley and D. Prendergast, *Phys. Rev. Lett.*, 2017, **118**, 096402.
14. W. Kohn and L. J. Sham, *Phys. Rev.*, 1965, **140**, A1133-A1138.
15. P. Hohenberg and W. Kohn, *Phys. Rev.*, 1964, **136**, B864-B871.
16. A. H. England, A. M. Duffin, C. P. Schwartz, J. S. Uejio, D. Prendergast and R. J. Saykally, *Chem. Phys. Lett.*, 2011, **514**, 187-195.
17. S. Roychoudhury, R. Qiao, Z. Zhuo, Q. Li, Y. Lyu, J.-H. Kim, J. Liu, E. Lee, B. J. Polzin, J. Guo, S. Yan, Y. Hu, H. Li, D. Prendergast and W. Yang, *Energy Environ. Mater.*, 2021, **4**, 246-254.
18. P. Giannozzi, S. Baroni, N. Bonini, M. Calandra, R. Car, C. Cavazzoni, D. Ceresoli, G. L. Chiarotti, M. Cococcioni, I. Dabo, A. Dal Corso, S. de Gironcoli, S. Fabris, G. Fratesi, R. Gebauer, U. Gerstmann, C. Gougoussis, A. Kokalj, M. Lazzeri, L. Martin-Samos, N. Marzari, F. Mauri, R. Mazzarello, S. Paolini, A. Pasquarello, L. Paulatto, C. Sbraccia, S. Scandolo, G. Sclauzero, A. P. Seitsonen, A. Smogunov, P. Umari and R. M. Wentzcovitch, *J. Phys.: Condens. Matter*, 2009, **21**, 395502.
19. J. P. Perdew, K. Burke and M. Ernzerhof, *Phys. Rev. Lett.*, 1996, **77**, 3865-3868.
20. J. P. Perdew, K. Burke and Y. Wang, *Phys. Rev. B.*, 1996, **54**, 16533-16539.
21. D. Vanderbilt, *Phys. Rev. B*, 1990, **41**, 7892-7895.
22. N. Kayunkid, S. Uttiya and M. Brinkmann, *Macromolecules*, 2010, **43**, 4961-4967.
23. D. A. Outka, J. Stöhr, J. P. Rabe and J. D. Swalen, *J. Chem. Phys.*, 1988, **88**, 4076-4087.
24. D. Dudenko, A. Kiersnowski, J. Shu, W. Pisula, D. Sebastiani, H. W. Spiess and M. R. Hansen, *Angew. Chem. Int. Ed.*, 2012, **51**, 11068-11072.